

# Distributed Koopman Operator Learning for Perception and Safe Navigation

Ali Azarbahram, Shenyu Liu and Gian Paolo Incremona, *Senior Member, IEEE*

**Abstract**—This paper presents a unified and scalable framework for predictive and safe autonomous navigation in dynamic transportation environments by integrating model predictive control (MPC) with distributed Koopman operator learning. High-dimensional sensory data are employed to model and forecast the motion of surrounding dynamic obstacles. A consensus-based distributed Koopman learning algorithm enables multiple computational agents or sensing units to collaboratively estimate the Koopman operator without centralized data aggregation, thereby supporting large-scale and communication-efficient learning across a networked system. The learned operator predicts future spatial densities of obstacles, which are subsequently represented through Gaussian mixture models. Their confidence ellipses are approximated by convex polytopes and embedded as linear constraints in the MPC formulation to guarantee safe and collision-free navigation. The proposed approach not only ensures obstacle avoidance but also scales efficiently with the number of sensing or computational nodes, aligning with cooperative perception principles in intelligent transportation system (ITS) applications. Theoretical convergence guarantees and predictive constraint formulations are established, and extensive simulations demonstrate reliable, safe, and computationally efficient navigation performance in complex environments.

**Index Terms**—Koopman operator, model predictive control, distributed learning, data-driven modeling, dynamic obstacle avoidance.

## I. INTRODUCTION

The advent of intelligent transportation systems (ITS) has driven increasing interest in autonomous agents that can safely navigate in dynamic, uncertain environments such as urban streets, plazas, and shared pedestrian zones [1]. In these settings, safety and reliability become paramount [2]. Ground robots or autonomous platforms moving through cluttered, time-varying environments must continuously account for surrounding obstacles, adapt to uncertainty, and rapidly incorporate new sensory information [3]. Among control methodologies, model predictive control (MPC) stands out for ITS-related applications by optimizing trajectories while enforcing constraints such as collision avoidance and kinematic limits [4]–[6].

Avoiding collisions with moving targets such as vehicles, pedestrians, or crowds is a central concern in ITS appli-

cations. Considerable work has addressed static obstacles (see e.g., [7], [8]), but dynamic obstacle avoidance remains more challenging due to unpredictability, interaction effects, and environmental uncertainty [9]–[11]. In transportation settings, predictions of pedestrian flows [12], [13] or vehicle trajectories [14], [15] over short horizons become critical. Indeed, those forecasts directly influence the control decisions in a receding-horizon framework. As a result, prediction-aware MPC formulations, where predicted obstacle regions are incorporated as time-varying constraints, have grown in interest in robotics and ITS communities [10], [16], [17].

In real-world ITS deployments, perception is often achieved through high-dimensional sensing modalities such as cameras, radar, or LiDAR units mounted on vehicles, roadside units, or drones [18]. Extracting and modeling dynamic behavior of obstacles from such data is nontrivial, especially when explicit motion models are unknown or unreliable. A natural remedy is to treat the environment as a spatiotemporal density field e.g., occupancy, flow, or intensity maps, and to learn predictive models directly from raw sensor sequences. This shift toward data-driven forecasting enables better handling of complex, non-Newtonian motion patterns (e.g. crowds, group flows) as probabilistic density predictions [19], which aligns well with ITS needs such as trajectory prediction, flow forecasting, and shared autonomous navigation.

The Koopman operator framework forms a powerful backbone for such data-driven modeling. By lifting nonlinear dynamics into a function space, system evolution becomes linear in the space of observables [20]. This enables use of linear-system tools for nonlinear tasks like prediction, estimation, and control. In practice, finite-dimensional approximations of the Koopman operator are built from time-series data and have shown success in system identification, control, and spatiotemporal forecasting [20]–[24]. In ITS and robotics domains, Koopman-based methods have been applied to modeling [25], [26], planning [27], object tracking [28], robust control [29], and vehicular mobility systems [30], [31].

Nonetheless, most Koopman-learning methods remain centralized [23], [32], [33]. Centralized strategies require full access to the entire dataset at one location, an assumption that fails under ITS constraints, such as limited computational capabilities, distributed edge sensors, privacy rules, and bandwidth bottlenecks. Distributed Koopman learning addresses these limitations by allowing agents or computational nodes to compute local operator estimates and coordinate to form a shared global Koopman model. In our framework, high-dimensional sensory snapshots (e.g. partitions of camera im-

This research was funded by the Italian Ministry of Enterprises and Made in Italy for the project 4DDS (4D Drone Swarms) under grant no. F/310097/01-04/X56, and the National Natural Science Foundation of China under grant no. 62203053.

A. Azarbahram is with The Department of Electrical Engineering, Chalmers University of Technology, Gothenburg, 412 96, Sweden. (e-mail: ali.azarbahram@chalmers.se). S. Liu is with the School of Automation, Beijing Institute of Technology, China. (e-mail: shenyulu@bit.edu.cn). G. P. Incremona is with the Dipartimento di Elettronica, Informazione e Bioingegneria, Politecnico di Milano, 20133 Milan, Italy. (e-mails: gian-paolo.incremona@polimi.it)

ages) are processed in parallel across multiple computational nodes (virtual agents). Each agent works on its share of the lifted observables and participates in a consensus-based least-squares scheme to estimate the global Koopman operator without exchanging raw data. This mechanism enhances scalability, reduces communication overhead, and ensures adaptability. The resulting operator can then propagate high-dimensional sensory states forward in time to generate spatial density forecasts of dynamic obstacles.

Prior works have explored various distributed or scalable Koopman paradigms, yet important gaps persist in combining convergence, interpretability, and computational efficiency. The alternating minimization with neural liftings in [34] introduces nonconvexity and dictionary-based splitting. The neighborhood-based graph Koopman in [35] depends on known coupling structure and lacks a seamless least-squares consensus framework. The graph neural networks based geometric method in [36] trades off interpretability and incurs heavy communication overhead. Deep distributed Koopman methods (e.g. [37], [38]) enhance expressivity at the price of non-convexity and large communication. The sequential partitioning scheme in [39] handles temporal splits and ensures convergence to extended dynamic mode decomposition (EDMD), but fails to partition high-dimensional spatial data.

Here we propose a novel distributed Koopman learning algorithm where each node processes its local sensor data and collaborates in a consensus-based optimization over a communication graph to collectively recover the global Koopman operator. This approach preserves convexity and interpretability of EDMD while granting theoretical convergence to the centralized solution under mild connectivity and step-size conditions. By avoiding nonconvexity, raw data exchange, and high communication demands, it scales efficiently to high-dimensional lifted spaces, making it well suited for ITS-scale environments such as imaging, urban crowd flows, and vehicular sensing. It also complements prior temporal splitting schemes like [39], filling in the orthogonal dimension of data decomposition.

In recent literature, the Koopman operator framework has emerged as a promising paradigm for data-driven modeling and prediction of complex dynamical systems in robotic and transportation domains. In [40], the Koopman operator was first employed to model and forecast the motion of unknown moving obstacles in a single-agent unmanned aerial vehicle (UAV) navigation problem, providing a predictive mechanism for anticipatory path planning. Building on this idea, [41] extended the Koopman-based methodology to a cooperative multi-agent setting through distributed and switched MPC, enabling decentralized collision-free navigation of multiple UAVs in dynamic and uncertain environments.

In contrast to these prior works, the present study introduces, for the first time, a Koopman learning architecture that learns the dynamic obstacle model itself in a fully distributed manner. The learned distributed Koopman model is then integrated into an MPC framework for safe navigation in dynamic environments. Predicted obstacle densities are represented as Gaussian mixture models, converted

into confidence ellipses, and subsequently approximated by convex polytopes. These polytopic regions are incorporated as linear constraints within the MPC problem, ensuring collision avoidance and maintaining safety margins across the prediction horizon. Crucially, this perception-to-control pipeline is fully distributed where no centralized fusion is required, thus making it suitable for deployment in large-scale, dynamic, sensor-rich environments. This enables real-time, scalable deployment in large-scale, sensor-rich ITS applications, where distributed sensing and computation are essential for robust and safe autonomous operation.

The remainder of the paper is organized as follows. Section II presents the problem formulation and necessary preliminaries; Section III describes the distributed Koopman algorithm and its integration with MPC; Section IV presents simulation results validating the method; and Section V concludes the paper.

*Notations and definitions:* Throughout the paper,  $\mathbb{N}$ ,  $\mathbb{R}$ , and  $\mathbb{C}$  denote the sets of nonnegative integers, real numbers, and complex numbers, respectively. Vectors in  $\mathbb{R}^n$  and real matrices in  $\mathbb{R}^{n \times m}$  are written using the customary superscripts. The  $n \times n$  identity is  $I_n$ , while  $0_{n \times m}$  and  $1_{n \times m}$  are the all-zeros and all-ones matrices of size  $n \times m$ . When the size can be inferred, subscripts are omitted for brevity. Diagonal constructions use  $\text{diag}(\cdot)$ : for scalars  $a_1, \dots, a_p$  we write  $\text{diag}(a_1, \dots, a_p)$ , and for blocks  $A_1, \dots, A_p$  we use  $\text{diag}(A_1, \dots, A_p)$ . The Kronecker product is  $A \otimes B$ , and matrix transpose is  $A^\top$ . For a square matrix  $A \in \mathbb{R}^{n \times n}$ , we use  $\det(A)$  for the determinant,  $\text{tr}(A)$  for the trace, and  $\Lambda(A)$  for the spectrum (set of eigenvalues). If  $\lambda \in \mathbb{C}$ , its real and imaginary parts are denoted by  $\text{Re}(\lambda)$  and  $\text{Im}(\lambda)$ . For vectors  $x \in \mathbb{R}^n$ , the Euclidean norm is  $\|x\|$ . For matrices  $A \in \mathbb{R}^{m \times n}$ , the Frobenius norm is  $\|A\|_F := \text{tr}(A^\top A)$ .

Let  $\mathcal{G} = (\mathcal{P}, \mathcal{E})$  be an undirected graph with node set  $\mathcal{P} := \{1, \dots, p\}$ ,  $p \in \mathbb{N}$ , and edge set  $\mathcal{E} \subseteq \mathcal{P} \times \mathcal{P}$ . An edge  $(i, j) \in \mathcal{E}$  implies the reciprocal edge  $(j, i) \in \mathcal{E}$ . A *path* is a sequence of nodes linked by edges; the graph is *connected* if every pair of nodes is joined by some path. For each node  $i \in \mathcal{P}$ , its neighborhood is  $N(i) := \{j \in \mathcal{P} : (i, j) \in \mathcal{E}\}$ . The Laplacian matrix associated with graph  $\mathcal{G}$  is  $L = [L_{ij}] \in \mathbb{R}^{p \times p}$ , defined elementwise by

$$L_{ij} = \begin{cases} -1, & \text{if } (i, j) \in \mathcal{E}, i \neq j, \\ 0, & \text{if } (i, j) \notin \mathcal{E}, i \neq j, \\ -\sum_{k \neq i} L_{ik}, & \text{if } i = j. \end{cases}$$

## II. PRELIMINARIES AND PROBLEM STATEMENT

In this section, first the considered robot model is introduced and then the safe navigation control problem is formulated.

### A. Unicycle robot model and feedback linearization

The unicycle robot model is adopted as a representative abstraction of wheeled autonomous ground vehicles widely

studied in ITS communities. Its dynamics capture the essential nonholonomic motion constraints of cars, delivery robots, and small-scale urban service platforms, while remaining analytically tractable for control design and verification. This simplified model provides a canonical testbed for developing and validating predictive control strategies in dynamic traffic-like settings, where motion feasibility, safety margins, and real-time trajectory planning are critical. Beyond ground vehicles, the same modeling principles extend naturally to other nonholonomic platforms such as mobile robots and automated guided vehicles used in cooperative transportation and urban mobility networks. The considered kinematics model of the unicycle robot is captured by the nonlinear system

$$\begin{cases} \dot{x} = v \cos \theta, \\ \dot{y} = v \sin \theta, \\ \dot{\theta} = \omega, \\ \dot{v} = a, \end{cases} \quad (1)$$

where the state  $(x, y, \theta)$  encodes the global position and orientation, and the control variables are the linear acceleration  $a$  and angular velocity  $\omega$ . The parameter  $v$  denotes the linear velocity.

To obtain a linear structure suitable for control, a feedback linearization scheme [42] is adopted. Introducing the transformed coordinates

$$\eta_1 = x, \quad \eta_2 = \dot{x}, \quad \eta_3 = y, \quad \eta_4 = \dot{y},$$

the dynamics in terms of  $\eta_i$ ,  $i = 1, 2, 3$  becomes

$$\dot{\eta}_1 = \eta_2, \quad (2a)$$

$$\dot{\eta}_2 = a \cos \theta - v\omega \sin \theta, \quad (2b)$$

$$\dot{\eta}_3 = \eta_4, \quad (2c)$$

$$\dot{\eta}_4 = a \sin \theta + v\omega \cos \theta. \quad (2d)$$

By defining auxiliary control inputs

$$a_x = a \cos \theta - v\omega \sin \theta, \quad a_y = a \sin \theta + v\omega \cos \theta,$$

the system is recast into two decoupled double integrators. The mapping back to the original inputs is recovered via

$$\begin{bmatrix} \omega \\ a \end{bmatrix} = \frac{1}{v} \begin{bmatrix} -\sin \theta & \cos \theta \\ v \cos \theta & v \sin \theta \end{bmatrix} \begin{bmatrix} a_x \\ a_y \end{bmatrix}, \quad (3)$$

which is valid provided  $v \neq 0$ . This singularity must be considered during controller implementation as emphasized in [42].

Let now the state of the linearized representation be  $\mathbf{x}_t = [\eta_1, \eta_2, \eta_3, \eta_4]^\top$ . Its discrete-time evolution is modeled as

$$\mathbf{x}_{t+1} = A\mathbf{x}_t + B\mathbf{u}_t, \quad (4)$$

with input vector  $\mathbf{u}_t = [a_x, a_y]^\top$ . The system matrices are

$$A = \begin{bmatrix} 1 & \tau & 0 & 0 \\ 0 & 1 & 0 & 0 \\ 0 & 0 & 1 & \tau \\ 0 & 0 & 0 & 1 \end{bmatrix}, \quad B = \begin{bmatrix} \frac{\tau^2}{2} & 0 \\ \tau & 0 \\ 0 & \frac{\tau^2}{2} \\ 0 & \tau \end{bmatrix},$$

where  $\tau$  is the sampling interval.

The Cartesian position of the robot, required for reference tracking and obstacle avoidance, is obtained through

$$\mathbf{z}_t = C\mathbf{x}_t, \quad (5)$$

where

$$C = \begin{bmatrix} 1 & 0 & 0 & 0 \\ 0 & 0 & 1 & 0 \end{bmatrix}.$$

This discretized and feedback-linearized formulation provides the predictive model used within the MPC framework described in the subsequent section.

### B. Problem statement

We address the challenge of safe and predictive navigation in dynamic environments through the integration of distributed perception and MPC. Aerial images captured by a downward-facing camera provide high-dimensional spatiotemporal observations of surrounding moving obstacles, such as pedestrians and vehicles. The motion of these obstacles is modeled using a Koopman operator framework, which lifts the underlying nonlinear dynamics into a higher-dimensional linear space, enabling tractable prediction and analysis. To efficiently process the high-dimensional sensory data, a distributed Koopman learning scheme is employed in which each image snapshot is treated through multiple computational nodes. These local computation nodes collaboratively estimate the Koopman operator via a consensus-based optimization procedure, eliminating the need for centralized computation while preserving global model consistency. The learned operator is then used to forecast future obstacle density maps, which are represented as Gaussian mixture models and converted into convex polytopic regions through confidence ellipses. These predicted regions are incorporated into an MPC formulation governing the motion of a unicycle robot, where they act as time-varying linear constraints to ensure collision-free and anticipatory motion planning. The proposed framework thus enables scalable, cooperative, and perception-driven decision-making suitable for real-time navigation in complex, dynamic, and partially observed transportation environments.

## III. MAIN RESULTS

In this section the proposed perception-to-control architecture is introduced. Given the goal position  $\mathbf{z}^*$  and the prediction horizon  $H$ , the task of the MPC controller is to ensure that the actual state and control input of the robot remain close to their reference counterparts while fulfilling all dynamic, actuation, and safety constraints derived from the environment perception model. The optimization problem

is formally stated as follows:

$$\min_{\bar{z}_t, \bar{u}_t} \sum_{h=0}^{H-1} \|z_{t+h|t} - z^*\|_Q^2 + \|u_{t+h|t}\|_R^2 \quad (6a)$$

$$\text{s.t.} \quad \begin{cases} x_{t+h+1|t} = Ax_{t+h|t} + Bu_{t+h|t}, \\ z_{t+h|t} = Cx_{t+h|t}, \quad \forall h = 0, \dots, H-1, \end{cases} \quad (6b)$$

$$x_{t|t} = x_t, \quad (6c)$$

$$\Omega_{t+h,\ell|t}^* z_{t+h|t} \geq \varrho_{t+h,\ell|t}^* + \varepsilon, \quad \forall h = 0, \dots, H-1, \quad \forall \ell = 1, \dots, L_o, \quad (6d)$$

where  $(\bar{z}_t, \bar{u}_t) =: (z_{t:t+H-1|t}, u_{t:t+H-1|t})$ . The symmetric positive matrices  $Q$  and  $R$  include weighting coefficients that balance tracking accuracy against control effort, ensuring smooth and stable behavior. The initial condition of the optimization problem is set in (6c) and the constraints in (6d) are incorporated to guarantee obstacle-free trajectories by restricting the predicted robot positions within admissible safe regions. While the specific structure of the parameters  $\Omega_{t+h,\ell|t}^*$ ,  $\varrho_{t+h,\ell|t}^*$ ,  $L_o$ , and  $\varepsilon$  will be rigorously defined in the subsequent sections, it is worth noting that these terms are derived directly from distributively learned Koopman-based predictions of dynamic obstacle motion. Each constraint represents a linearized safety boundary that evolves in time based on the learned dynamics, thus transforming high-dimensional sensory forecasts into computationally efficient linear inequalities. This tight integration between perception and control ensures that the MPC simultaneously reasons about goal tracking and future obstacle motion, setting the foundation for a predictive, adaptive navigation strategy.

The optimal control sequence obtained from solving (6), denoted by  $(\bar{z}_t^*, \bar{u}_t^*)$ , defines the desired trajectories over the prediction horizon, while only the first control input  $u_{t|t}^*$  is executed at each time step according to the receding horizon principle.

#### A. Distributed Koopman modeling of dynamic obstacles

The Koopman operator framework provides a linear representation of nonlinear dynamical systems by acting on functions of the state rather than the state itself. Consider the discrete-time nonlinear system

$$x_{k+1} = f(x_k), \quad x_k \in \mathcal{M} \subseteq \mathbb{R}^q, \quad (7)$$

where the mapping  $f : \mathcal{M} \rightarrow \mathcal{M}$  is nonlinear and  $q$  denotes the state dimension. Instead of analyzing the state trajectory  $\{x_k\}$ , one studies the evolution of observables  $\phi : \mathcal{M} \rightarrow \mathbb{R}$  belonging to a Hilbert space  $\mathcal{H}$  of scalar-valued functions. The infinite-dimensional Koopman operator  $\mathcal{K} : \mathcal{H} \rightarrow \mathcal{H}$  is introduced as

$$(\mathcal{K}\phi)(x) = \phi(f(x)), \quad \forall \phi \in \mathcal{H}, x \in \mathcal{M}. \quad (8)$$

Although  $f$  is nonlinear, the operator  $\mathcal{K}$  acts linearly on the space of observables. To approximate its action in finite dimensions, we select  $n$  observables and group them into the vector-valued mapping

$$\Phi(x) = [\phi_1(x), \phi_2(x), \dots, \phi_n(x)]^\top \in \mathbb{R}^n, \quad (9)$$

which lifts each state  $x \in \mathcal{M}$  into an  $n$ -dimensional feature space [23]. With a dataset of  $N$  samples  $\{x_k, f(x_k)\}_{k=1}^N$ , the lifted snapshots are organized as

$$X = [\phi(x_1), \phi(x_2), \dots, \phi(x_N)] \in \mathbb{R}^{n \times N}, \quad (10)$$

$$Y = [\phi(f(x_1)), \phi(f(x_2)), \dots, \phi(f(x_N))] \in \mathbb{R}^{n \times N}. \quad (11)$$

The EDMD [23] provides a tractable approximation by projecting the action of  $\mathcal{K}$  onto the span of the chosen observables. This yields a finite matrix  $K \in \mathbb{R}^{n \times n}$  such that the lifted states evolve approximately according to

$$Y \approx KX. \quad (12)$$

The optimal approximation is obtained from the Frobenius-norm least-squares problem

$$K^* = \arg \min_{K \in \mathbb{R}^{n \times n}} \|Y - KX\|_F^2, \quad (13)$$

which provides a finite-dimensional representation of the Koopman operator consistent with the available data.

To enable predictive and safe robot navigation, it is essential to model the motion of unknown moving obstacles without explicit dynamics. We adopt a Koopman operator framework that lifts nonlinear dynamics into a linear space using high-dimensional perceptual data (e.g., images or video snapshots) collected over time. These snapshots capture the spatiotemporal distribution of obstacles and serve as the training data for learning the Koopman operator. Due to the high dimensionality of the data, centralized learning becomes computationally infeasible for real-time updates. To address this, we propose a distributed Koopman learning approach, where snapshot data is investigated using multiple computational nodes (virtual agents). Each node processes local lifted observables and collaboratively contributes to a globally consistent Koopman model via consensus updates. This parallel architecture enables scalable, timely learning suitable for integration into real-time obstacle-aware navigation systems.

In the considered setting, each node  $i \in \{1, \dots, p\}$  has access only to a local segment of the lifted observables and their forward-time transitions, i.e.,  $X_i \in \mathbb{R}^{n_i \times N}$  and  $Y_i \in \mathbb{R}^{n_i \times N}$ , where  $\sum_{i=1}^p n_i = n$ . Formally, this local partitioning can be expressed globally as

$$X = \begin{bmatrix} X_1 \\ \vdots \\ X_p \end{bmatrix}, \quad Y = \begin{bmatrix} Y_1 \\ \vdots \\ Y_p \end{bmatrix}.$$

This structure reflects practical scenarios where agents collect or process data from disjoint spatial regions or sensor domains, leading to decentralized data ownership. Each agent aims to collaboratively solve the least-squares problem (13) while only accessing its local data and communicating with its neighbors over a connected undirected graph  $\mathcal{G}$ . The design objective is for each agent  $i$  to compute its corresponding block-column of the global Koopman operator  $K$ , denoted as  $K_i \in \mathbb{R}^{n \times n_i}$ , by leveraging distributed optimization and consensus over  $\mathcal{G}$ , thereby achieving global Koopman operator learning without central data aggregation.

---

**Algorithm 1** Distributed Koopman Operator Learning

---

**Input:**  $\alpha$  satisfying  $\alpha < \alpha_{\max}$  from (28).

- 1: Initialize arbitrary  $K_i(0) \in \mathbb{R}^{n \times n_i}$ ,  $S_i(0) \in \mathbb{R}^{n \times N}$  for all  $i \in \mathcal{P}$  according to (15).
- 2: **loop** for  $t = 0, 1, \dots, t_{\max} - 1$ , the  $i$ -th agent,  $i \in \mathcal{P}$
- 3:   Broadcast  $S_i(t)$  to its neighbors.
- 4:   Compute  $K_i(t+1), S_i(t+1)$  according to (14).
- 5: **end loop**

**Output:**  $K(t_{\max}) = [K_1(t_{\max}) \ \cdots \ K_p(t_{\max})]$ .

---

The group of nodes (virtual agents) aims to solve the problem (13) by a distributed algorithm as

$$K_i^+ = K_i - \alpha S_i X_i^\top, \quad (14a)$$

$$S_i^+ = S_i + (K_i^+ - K_i) X_i - \alpha \sum_{j \in N(i)} (S_i - S_j). \quad (14b)$$

Here,  $\alpha > 0$  is a discretization step-size and  $S_i \in \mathbb{R}^{n \times N}$  is another internal augmented state variable owned by the  $i$ -th agent for facilitating the convergence. The variables  $K_i, S_i$  start from the specific initial conditions

$$K_i(0) = 0, \quad S_i(0) = -Y_i \quad \forall i \in \mathcal{P}, \quad (15)$$

where  $Y_i \in \mathbb{R}^{n \times N}$  is the  $i$ -th block-column of the block-diagonal matrix

$$Y := \text{diag}(Y_1, \dots, Y_p) \in \mathbb{R}^{n \times Np}. \quad (16)$$

The convergence of the algorithm (14) is related to the eigenvalues of the following matrix

$$M := - \begin{bmatrix} X X^\top & X L \\ X^\top & L \end{bmatrix} \in \mathbb{R}^{(Np+n) \times (Np+n)}, \quad (17)$$

where

$$X = \text{diag}(X_1, \dots, X_p) \in \mathbb{R}^{n \times Np}, \quad (18)$$

$$L = L \otimes I_N \in \mathbb{R}^{Np \times Np}, \quad (19)$$

and  $L$  is the Laplacian matrix of  $\mathcal{G}$ . The distributed algorithm for Koopman operator learning is summarized in Algorithm 1. Before introducing the main result in Theorem 1, the following lemma is instrumental.

**Lemma 1.**  $K^* \in \mathbb{R}^{n \times n}$  is an optimal solution to the problem (13) if and only if there exists  $W^* \in \mathbb{R}^{n \times Np}$  such that  $(K^*, W^*)$  is an optimal solution to the constrained problem

$$\min_{K, W} \|Y - KX - W\|^2, \quad (20a)$$

$$\text{subject to } W(1_p \otimes I_N) = 0, \quad (20b)$$

where  $Y, X$  are defined in (16), (18).

*Proof.* Define the Lagrangian

$$\mathcal{L}(K, W, \Lambda) = \frac{1}{2} \|Y - KX - W\|^2 + \text{tr}(\Lambda^\top W(1_p \otimes I_N)),$$

where  $\Lambda \in \mathbb{R}^{n \times Np}$  is the matrix of Lagrangian multipliers. Note that the optimization problem (20) is convex; hence by

the KKT condition [43],  $(K^*, W^*) \in \mathbb{R}^{n \times n} \times \mathbb{R}^{n \times Np}$  is an optimal solution to (20) if and only if for some  $\Lambda^* \in \mathbb{R}^{n \times Np}$ ,

$$\frac{\partial \mathcal{L}}{\partial K}(K^*, W^*, \Lambda^*) = -(Y - K^* X - W^*) X^\top = 0, \quad (21)$$

$$\frac{\partial \mathcal{L}}{\partial W}(K^*, W^*, \Lambda^*) = -(Y - K^* X - W^*) + \Lambda^* (1_p^\top \otimes I_N) = 0, \quad (22)$$

$$\frac{\partial \mathcal{L}}{\partial \Lambda}(K^*, W^*, \Lambda^*) = W^* (1_p \otimes I_N) = 0. \quad (23)$$

From (22),

$$W^* = Y - K^* X - \Lambda^* (1_p^\top \otimes I_N). \quad (24)$$

Substituting into (23), we obtain

$$(Y - K^* X)(1_p \otimes I_N) = \Lambda^* (1_p^\top \otimes I_N)(1_p \otimes I_N) = p \Lambda^*.$$

Therefore,

$$\Lambda^* = \frac{1}{p} (Y - K^* X)(1_p \otimes I_N)$$

which, after substituting into (24), gives

$$W^* = (Y - K^* X) \left( I_{Np} - \frac{1}{p} (1_p 1_p^\top) \otimes I_N \right).$$

Substituting into (21), we conclude that

$$\frac{1}{p} (Y - K^* X) ((1_p 1_p^\top) \otimes I_N) X^\top = 0. \quad (25)$$

In other words,  $K^*$  needs to be such that  $(Y - K^* X)$  is orthogonal to  $X ((1_p 1_p^\top) \otimes I_N)$ .

On the other hand, note that the optimization problem (13) can be equivalently written as

$$\min_K \|(Y - KX)(1_p \otimes I_n)\|^2, \quad (26)$$

which is also convex. Hence, the first order condition,

$$(Y - K^* X)(1_p \otimes I_n)(1_p \otimes I_n) X^\top = 0, \quad (27)$$

is both necessary and sufficient for optimality. Because (27) is the same as (25), Lemma 1 is proven.  $\square$

We are now in a position to introduce the following theorem.

**Theorem 1.** Suppose the communication graph  $\mathcal{G}$  is undirect and connected. There exists

$$\alpha_{\max} := - \max_{\lambda \in \Lambda(M) \setminus \{0\}} \frac{2 \text{Re}(\lambda)}{|\lambda|^2} > 0, \quad (28)$$

such that as long as the step size  $\alpha < \alpha_{\max}$ , the matrix

$$K = [K_1 \ \cdots \ K_p] \quad (29)$$

given by (14) starting from initial conditions (15) will converge to an optimal solution for the problem (13). Furthermore, the convergence is exponential with rate  $\rho > \rho_{\max}$ , where

$$\rho_{\max} := \max_{\lambda \in \Lambda(M) \setminus \{0\}} \sqrt{1 + 2\alpha \text{Re}(\lambda) + \alpha^2 |\lambda|^2}. \quad (30)$$

*Proof.* Define

$$\begin{aligned} W &= S + \mathbf{Y} - K\mathbf{X}, \\ e_K &= K - K^*, \quad e_W = W - W^*. \end{aligned}$$

It follows from (14a) and (21) that

$$\begin{aligned} e_K^+ &= K^+ - K^* \\ &= K - \alpha S \mathbf{X}^\top - K^* \\ &= e_K + \alpha(\mathbf{Y} - K\mathbf{X} - W)\mathbf{X}^\top \\ &= e_K + \alpha(\mathbf{Y} - (e_K + K^*)\mathbf{X} - (e_W + W^*))\mathbf{X}^\top \\ &= e_K - \alpha(e_K\mathbf{X} + e_W)\mathbf{X}^\top. \end{aligned}$$

Meanwhile, Because the graph  $\mathcal{G}$  is connected,  $\mathbf{1}_p^\top L = 0$ . Thus (22) implies  $(\mathbf{Y} - K^*\mathbf{X} - W^*)\mathbf{L} = 0$ , where recall  $\mathbf{L}$  is defined by (19). Hence it follows from (14b) that

$$\begin{aligned} e_W^+ &= W^+ - W^* \\ &= S^+ + \mathbf{Y} - K^+\mathbf{X} - W^* \\ &= S + (K^+ - K)\mathbf{X} + \alpha(\mathbf{Y} - K\mathbf{X} - W)\mathbf{L} \\ &\quad + \mathbf{Y} - K^+\mathbf{X} - W^* \\ &= S + \mathbf{Y} - K\mathbf{X} + \alpha(\mathbf{Y} - K\mathbf{X} - W)\mathbf{L} - W^* \\ &= W + \alpha(\mathbf{Y} - K\mathbf{X} - W)\mathbf{L} - W^* \\ &= e_W + \alpha(\mathbf{Y} - (e_K + K^*)\mathbf{X} - (e_W + W^*))\mathbf{L} \\ &= e_W - \alpha(e_K\mathbf{X} + e_W)\mathbf{L}. \end{aligned}$$

Because of the initial conditions (15),  $W(0) = 0$ , which implies  $e_W(0) = -W^*$ . Therefore,  $e_W(k)(\mathbf{1}_p \otimes I_N) = 0$  for all  $k \in \mathbb{N}$ . In summary, we have

$$\begin{bmatrix} e_K^+ & e_W^+ \end{bmatrix} = \begin{bmatrix} e_K & e_W \end{bmatrix} (I + \alpha \mathbf{M}), \quad (31)$$

where recall  $\mathbf{M}$  is defined in (17). It can be verified that  $\mathbf{M}$  is semi-Hurwitz. Hence when  $\alpha < \alpha_{\max}$ , where  $\alpha_{\max}$  is defined in (28),  $I + \alpha \mathbf{M}$  is semi-Schur. Consequently, by [44, Corollary 3],  $\begin{bmatrix} e_K & e_W \end{bmatrix} \rightarrow \begin{bmatrix} e_K^\infty & e_W^\infty \end{bmatrix}$  exponentially fast, such that  $\begin{bmatrix} e_K^\infty & e_W^\infty \end{bmatrix} \mathbf{M} = 0$ . This implies that

$$\begin{aligned} (e_K^\infty \mathbf{X} + e_W^\infty)\mathbf{X}^\top &= 0, \\ (e_K^\infty \mathbf{X} + e_W^\infty)\mathbf{L} &= 0. \end{aligned}$$

Making reference to (21)-(23), we see that the limit

$$\lim_{k \rightarrow \infty} \begin{bmatrix} K(k) & W(k) \end{bmatrix} = \begin{bmatrix} K^* & W^* \end{bmatrix} + \begin{bmatrix} e_K^\infty & e_W^\infty \end{bmatrix}$$

also satisfies the KKT condition for the problem (20). Hence by Lemma 1,  $\lim_{k \rightarrow \infty} K(k)$  is an optimal solution to the problem (13) and the convergence is exponentially fast.  $\square$

### B. Obstacle prediction and constraint formulation for MPC

The distributed Koopman learning algorithm introduced earlier serves as the foundation for prediction-based obstacle avoidance.

To clarify the Koopman prediction process, the paired matrices  $X$  and  $Y$  encode the temporal transitions of the spatial density field observed by the robot or aerial sensor. Once the distributed Koopman operator  $K$  is estimated, it serves as a linear propagator:

$$X_{t+h} \approx K^h X_t, \quad h = 1, 2, \dots, H.$$

Repeated application of  $K$  to the latest lifted snapshot yields a sequence of predicted lifted states, which are mapped back to the spatial domain to reconstruct predicted density maps  $\rho_{t+h}$ ,  $h = 1, 2, \dots, H$ . These maps represent the expected evolution of the dynamic obstacles over the MPC horizon. This procedure effectively translates temporal patterns captured from prior data into forward predictions of spatial occupancy, forming the basis for subsequent Gaussian mixture modeling and polytope-based constraint formulation.

Therefore, using the distributed Koopman operator  $K$ , we propagate lifted observables forward, reconstructing a sequence of density maps  $\{\rho_t\}_{t=1}^H$  over a 2D grid. Each  $\rho_t$  encodes predicted obstacle distributions. Thresholding  $\rho_t$  at  $c_\rho$  yields:

$$\Psi_t = \{\xi \in \mathbb{R}^2 : \rho_t(\xi) > c_\rho\}.$$

We fit a  $L_o$ -component Gaussian mixture model to  $\Psi_t$ , where each component  $\mathcal{N}(\xi \mid \mu_\ell, \Sigma_\ell)$  models a local obstacle as an ellipse.

Each Gaussian mixture model component defines an elliptical region:

$$\mathcal{C}_\ell = \{\xi : (\xi - \mu_\ell)^\top \Sigma_\ell^{-1} (\xi - \mu_\ell) \leq \delta^2\},$$

with  $\delta^2$  set by a chi-squared quantile. Decomposing  $\Sigma_\ell = UDU^\top$ , the semi-axes are:

$$\check{a}_\ell = \sqrt{\delta^2 \lambda_1}, \quad \check{b}_\ell = \sqrt{\delta^2 \lambda_2}.$$

Together with rotation  $U$ , these parameters fully describe  $\mathcal{C}_\ell$ . To form linear MPC constraints, we approximate  $\mathcal{C}_\ell$  by a polytope with  $n_\varsigma$  half-spaces (supporting hyperplanes).

Koopman-based forecasts produce time-indexed spatial density maps that are compressed into polytopes via confidence contours. Each polytope acts as a moving keep-out region; enforcing its most active supporting halfspace at each step is equivalent to shifting the robot's admissible output set away from predicted obstacles with a tunable margin. This converts perception into linear time-varying constraints that the MPC can handle natively, aligning the robot's feasible region with the anticipated flow of crowds. As a result, prediction and planning are tightly coupled: improved forecasts directly enlarge the feasible corridor, while conservative bounds still guarantee safety without destabilizing the optimizer.

For each angle  $\vartheta_\iota = 2\pi(\iota - 1)/n_\varsigma$ ,  $\iota = 1, \dots, n_\varsigma$ , we compute support points and normals:

$$s_\iota = \mu_\ell + U \begin{bmatrix} \check{a}_\ell \cos \vartheta_\iota \\ \check{b}_\ell \sin \vartheta_\iota \end{bmatrix}, \quad n_\iota = \begin{bmatrix} \cos \vartheta_\iota \\ \sin \vartheta_\iota \end{bmatrix}.$$

Each constraint becomes  $n_\iota^\top \xi \geq n_\iota^\top s_\iota + \varepsilon$ , and stacking gives:

$$\Omega_\ell \xi \geq \varrho_\ell + \varepsilon \mathbf{1}_{n_\varsigma},$$

with  $\Omega_\ell$  and  $\varrho_\ell$  collecting all normals and support values. At each MPC step  $t + h$ , for  $h = 1, \dots, H$ , and each obstacle  $\ell = 1, \dots, L_o$ , we enforce:

$$\Omega_{t+h,\ell} \xi_{t+h} \geq \varrho_{t+h,\ell} + \varepsilon \mathbf{1}_{n_\varsigma}.$$

To reduce complexity, we identify and enforce only the most active facet

$$\iota^* = \arg \max_{\iota} \left( \Omega_{t+h,\ell}^{(\iota)\top} \xi_{t+h} - \varrho_{t+h,\ell}^{(\iota)} - \varepsilon \right),$$

yielding:

$$\Omega_{t+h,\ell}^* := \Omega_{t+h,\ell}^{(\iota^*)\top}, \quad \varrho_{t+h,\ell}^* := \varrho_{t+h,\ell}^{(\iota^*)}.$$

These constraints are reformulated in terms of the MPC output  $z_{t+h|t}$ , resulting in the final avoidance condition:

$$\Omega_{t+h,\ell|t}^* z_{t+h|t} \geq \varrho_{t+h,\ell|t}^* + \varepsilon, \quad \forall h = 0, \dots, H-1, \quad \forall \ell = 1, \dots, L_o. \quad (32)$$

The safety margin  $\varepsilon \geq R_r$  accounts for the robot's size, ensuring robust obstacle avoidance.

#### IV. SIMULATION CASE-STUDY

The following four-stage simulation study demonstrates and investigates the full perception-to-control pipeline of our method.

##### A. Evaluation of distributed Koopman operator learning

The evaluation begins by characterizing the sensory snapshots used as input to the distributed Koopman learning algorithm. Each snapshot represents a two-dimensional grid of the environment, where entries take values in  $[0, 1]$  and encode normalized occupancy intensities: regions with values near 1 correspond to dense obstacle areas, while values close to 0 indicate free space. Thus, each snapshot compactly captures the spatial distribution of dynamic obstacles at a specific time, forming a high-dimensional state of the environment. Sequential snapshots collected over time constitute a temporal dataset describing the spatiotemporal evolution of moving obstacles. In the simulations, dynamic obstacle fields are generated over a  $30 \times 30$  spatial grid, observed through top-down camera snapshots recorded across  $N = 10$  time steps. Each frame depicts multiple moving obstacles with distinct initial densities and heterogeneous motion patterns, forming the dataset for distributed Koopman operator learning and subsequent prediction analysis.

The task is to reconstruct and predict the spatiotemporal evolution using  $p = 3$  nodes connected via a circular undirected communication graph. Each node holds local data

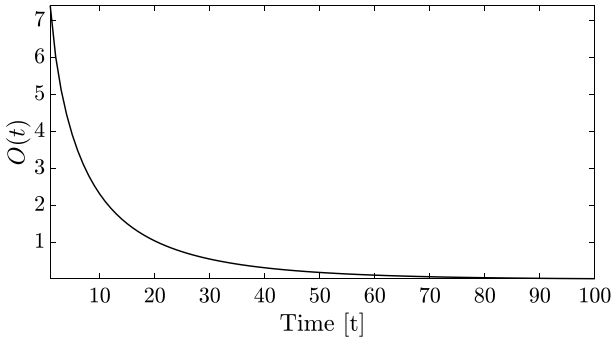


Fig. 1: Prediction discrepancy  $O(t)$  between distributed and centralized Koopman operators over iterations.

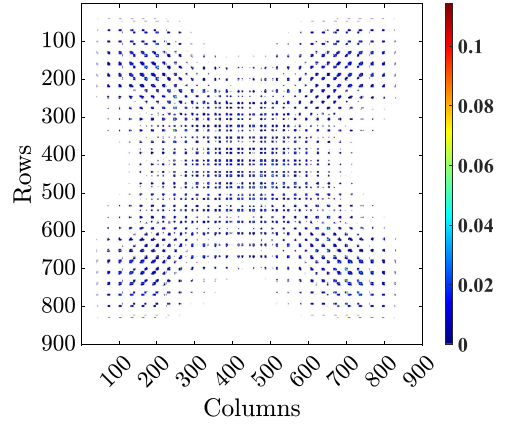


Fig. 2: Elementwise absolute difference between the distributed Koopman operator  $K_d$  and the centralized Koopman operator  $K^*$ .

matrices  $X_i, Y_i$ , as portions of the centralized matrices  $X, Y$  (with  $n = 900$  from grid vectorization). Then, each node estimates a local Koopman operator  $K_i \in \mathbb{R}^{n \times n_i}$ ,  $n_i = n/p$ , collectively approximating  $K \in \mathbb{R}^{n \times n}$ , via 100 optimization steps with neighbor communication. Using matrix  $M$  from (17), we compute  $\alpha_{\max} = 0.2095$  from (28) and set  $\alpha = 0.5\alpha_{\max}$ , yielding  $\rho_{\max} = 0.9185$  by (30).

Fig. 1 shows the evolution of the prediction discrepancy between distributed and centralized Koopman estimates, measured by the Frobenius norm:

$$O(t) := \|(K^* - K_d(t))X\|_F.$$

Here,  $K^*$  denotes the centralized Koopman operator derived from (13) and  $K_d(t)$  the distributed estimate at iteration  $t$ . The metric quantifies the difference in predicted lifted dynamics. As shown,  $O(t)$  decays exponentially, confirming convergence to the centralized solution. The convergence rate depends on the step size, graph Laplacian spectrum, and matrix  $X$ , with  $\rho_{\max} = 0.9185$ , validating the effectiveness of the distributed learning algorithm. Fig. 2 shows the entrywise absolute difference  $K_\Delta := |K_d - K^*|$ , with  $[K_\Delta]_{ij} := |[K_d]_{ij} - [K^*]_{ij}|$ . The heatmap reveals that most entries have small errors, indicating strong alignment

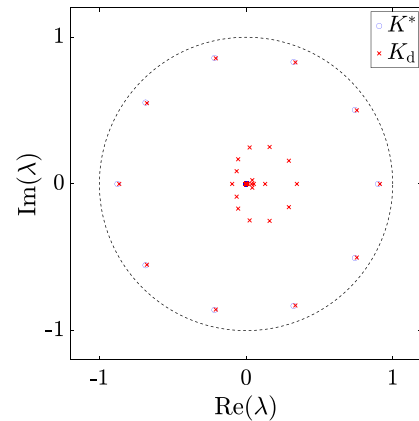


Fig. 3: Spectral comparison between the distributed Koopman operator  $K_d$  and the centralized Koopman operator  $K^*$ .



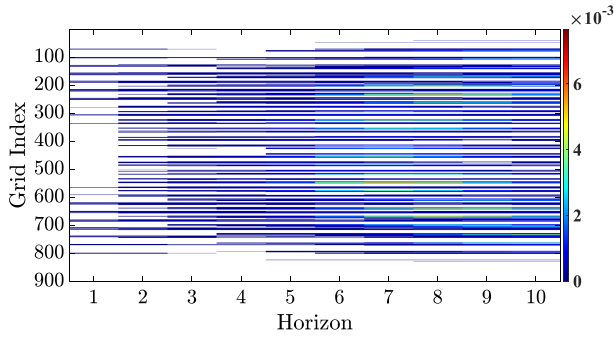


Fig. 4: Distributed error heatmap showing the absolute prediction error of the distributed Koopman operator  $K_d$  against the true system snapshots over the prediction horizon.

between distributed and centralized models. Block patterns reflect the partitioning across  $p = 3$  nodes, and higher deviations appear sparsely, likely due to local variations or communication limits. Fig. 3 compares eigenvalues of  $K^*$  (blue) and  $K_d$  (red) in the complex plane. All lie within the unit circle, confirming stability.  $K_d$ 's spectrum is slightly more spread but closely matches dominant modes of  $K^*$ , indicating successful preservation of key system dynamics via distributed learning. Fig. 4 depicts the prediction error of  $K_d$  over a  $30 \times 30$  spatial grid and prediction steps. Errors grow over time due to recursive forecasting, with some localized spikes likely from decentralized update limitations. This spatial-temporal map complements global metrics by revealing when and where prediction errors concentrate.

In the simulations, the lifting function is realized through direct vectorization of the spatial grid, where each pixel intensity of the snapshot is treated as an observable. This straightforward and non-parametric embedding ensures that the lifted state space coincides with the perceptual domain, preserving all spatial information prior to Koopman learning. Such direct lifting is particularly suitable for dynamic environments with unknown structure, as it avoids biases introduced by handcrafted features or predefined basis functions.

**Remark 1.** While alternative liftings (such as polynomial bases, radial or Fourier expansions, and neural observables) can improve representation capacity, they often increase design complexity and computational cost. Direct vectorization, by contrast, provides a fully data-driven baseline that captures the complete spatiotemporal variability in the observations, enabling a clear assessment of the scalability and convergence of the proposed distributed Koopman learning algorithm. Furthermore, since density values are already represented on the same grid, this lifting aligns naturally with the Gaussian mixture and polytope-based obstacle extraction pipeline, ensuring seamless integration between perception, learning, and prediction. For occupancy-like fields, direct vectorization yields a locality-preserving and interpretable lifting: each observable corresponds to a fixed spatial location, allowing the Koopman operator to encode transport and deformation patterns across neighboring pixels. This approach eliminates basis-mismatch issues and hyperparameter

tuning required by learned dictionaries or kernels, providing a lightweight, transparent, and computationally predictable embedding which results in well suited online updates and integration within the MPC loop.

**Remark 2.** The results in Fig. 1–4 demonstrate the progressive alignment of distributed Koopman estimates with the centralized reference solution over successive iterations. Initially, the estimate is suboptimal due to limited local information, but the consensus-based updates iteratively reduce this discrepancy, producing an exponential decay in the prediction error until near-equivalence with the centralized Koopman operator is achieved. The convergence rate is governed by the step size  $\alpha$ , the communication topology (via the Laplacian spectrum), and the conditioning of the lifted data matrices, encapsulated in  $\rho_{\max}$ . In online operation, the algorithm readily adapts to streaming or windowed data. When new observations become available, each agent updates its local matrices and resumes from the previous estimate rather than restarting from scratch [45]. This warm-start feature accelerates adaptation while preserving previously learned structure, ensuring that the suboptimality gap remains bounded and vanishes with continued iterations. Consequently, even intermediate solutions are sufficiently predictive for real-time deployment, while full consensus yields operators virtually identical to their centralized counterparts. This trade-off between adaptivity, convergence, and computational scalability makes the proposed approach suitable for continuous learning in dynamic, data-driven environments.

**Remark 3.** The convergence behavior of the distributed Koopman learning algorithm is closely tied to the parameters  $\rho_{\max}$  and  $\alpha$ . The value of  $\rho_{\max}$  depends on spectral properties of both the data matrices (in particular,  $\mathbf{X}$ ) and the communication graph Laplacian  $L$ , as seen in the expression of (30). Intuitively, richer and more informative data snapshots, as well as well-connected network topologies, reduce  $\rho_{\max}$  and improve convergence. The step-size  $\alpha$  acts as a design parameter: larger values can accelerate convergence initially but risk instability if chosen beyond the admissible range dictated by  $\rho_{\max}$ , while smaller values ensure stability but slow down the learning process. In practice,  $\alpha$  must be tuned to balance convergence speed and numerical robustness. These parameters thus directly influence both the transient prediction discrepancy (cf. Fig. 1) and the quality of the final Koopman approximation, especially in online settings where rapid adaptation to new data is critical.

## B. Comparison with other distributed Koopman methods

This subsection benchmarks the proposed distributed Koopman learning algorithm against representative methods from the literature to evaluate its performance under identical experimental conditions. For a consistent comparison, the same dataset, lifting function, and data partitions described earlier were used for the implementations in [34] and [35]. All methods operated on identical splits of the lifted matrices



$X$  and  $Y$ , and were evaluated using normalized one-step and multi-step trajectory prediction errors.

Results indicate that all distributed estimators closely approximate the centralized Koopman operator, confirming the general consistency of distributed EDMD formulations. To quantify performance, we define the normalized one-step and multi-step prediction errors as

$$e_1 = \frac{\|Y - K_d X\|_F}{\|Y - K^* X\|_F}, \quad e_h = \frac{\|Y^{(h)} - K_d^h X\|_F}{\|Y^{(h)} - (K^*)^h X\|_F},$$

where  $Y^{(h)}$  represents the  $h$ -step-ahead lifted data. These normalized quantities measure how closely the distributed approximation replicates the centralized Koopman model at different prediction horizons.

Numerical evaluations show that the one-step prediction errors remain close to unity for all distributed methods ( $e_1 \approx 1.01$ – $1.02$ ), indicating that all the proposed approaches reproduce the centralized Koopman predictions with only a marginal 1–2% deviation. For longer prediction horizons ( $h = 14$ , corresponding to the MPC planning window in the following section), we evaluate the relative performance among the distributed approaches. In this case, our proposed method achieves a normalized multi-step error approximately 11% – 13% smaller than those in [34] and [35]. This improvement reflects enhanced stability and reduced error accumulation when repeatedly applying the learned operator for multi-step forecasts. From a control standpoint, this superior multi-step accuracy is especially valuable: accurate long-horizon Koopman predictions enable the MPC to anticipate dynamic obstacle evolution more reliably, reducing constraint violations and ensuring smoother, safer navigation. Hence, even modest improvements in prediction consistency translate into tangible performance gains for the overall perception–control pipeline.

### C. MPC with Koopman-based dynamic obstacle avoidance

After validating the accuracy and convergence of the distributed Koopman operator in modeling dynamic obstacles, we integrate it into an MPC framework for safe robot navigation. The Koopman-based forecasts are exploited to construct time-varying polytopic constraints that guarantee collision-free trajectories over the prediction horizon while driving the robot toward its goal through smooth, feasible control actions.

The cost function in (6a) employs a prediction horizon  $H = 14$ , initial position  $z(0) = [0, 0]^\top$ , and target  $z^* = [15, 15]^\top$ . Dynamic obstacle avoidance is incorporated by approximating each Koopman-predicted elliptical region with a convex polytope defined by  $n_c = 8$  supporting hyperplanes as an effective trade-off between accuracy and computational cost. The linear inequalities of the form (32) are imposed at each horizon step, enforcing only the most active constraint per obstacle to ensure real-time feasibility while maintaining conservatism.

Fig. 5 shows the closed-loop trajectory in an environment with  $L_o = 12$  moving obstacle clusters where we observe that the robot reaches its target smoothly, maintaining safe

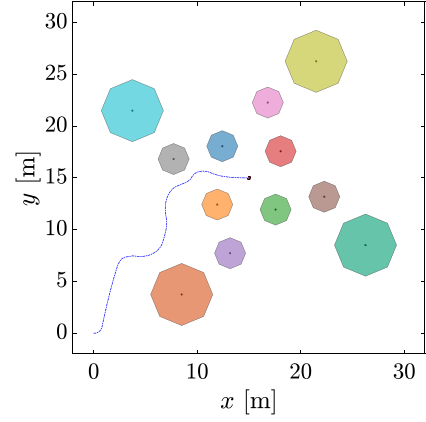
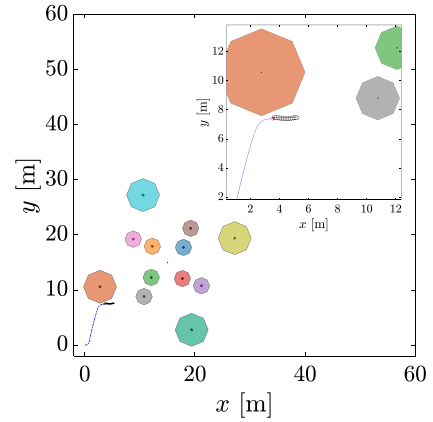
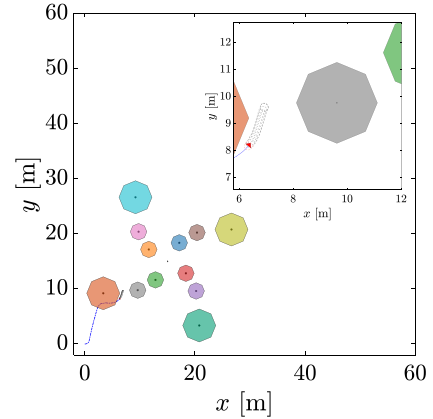


Fig. 5: The final robot trajectory with Koopman-predicted dynamic obstacle avoidance.



(a) Time = 15 [s].



(b) Time = 20 [s].

Fig. 6: Snapshots of robot and obstacle positions at different time instances.

separation by continuously adapting to predicted obstacle motion.

To further highlight predictive avoidance, Fig. 6 displays key snapshots during navigation. Each depicts the robot's orientation, predicted trajectory, and evolving obstacle regions, confirming proactive maneuvering guided by Koopman-based forecasts. The robot adjusts its path before collisions

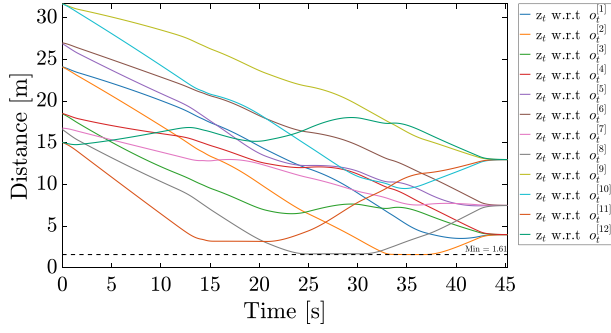


Fig. 7: Robot-to-obstacle distance over time.

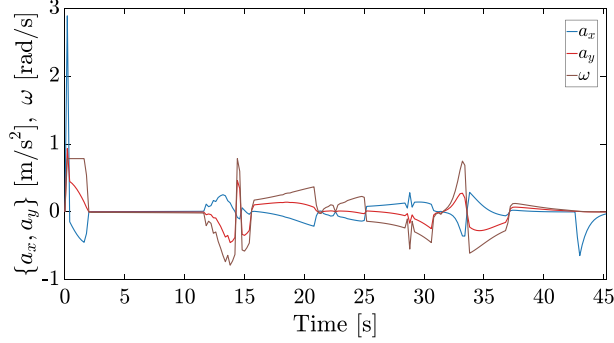


Fig. 8: Evolution of control inputs.

become imminent, demonstrating anticipatory control. Fig. 7 quantifies safety margins by plotting the Euclidean distance between the robot and each obstacle center. All distance profiles remain above the black dashed safety threshold, verifying consistent clearance and robust avoidance. This reinforces the predictive and conservative nature of the MPC policy. Lastly, Fig. 8 presents the control input profiles. The accelerations  $(a_x, a_y)$  govern translational dynamics, while the angular velocity  $\omega$  adjusts heading. These signals confirm dynamically feasible, well-coordinated actuation, validating that safe navigation is achieved through efficient integration of Koopman-based predictions within the MPC framework. For a detailed implementation guideline of Koopman-based moving obstacle avoidance MPC, the reader is referred to our recent work [40], where a complete prediction and control pipeline is developed and validated through a ROS2–Gazebo implementation.

**Remark 4.** *The scalability of the proposed framework stems from both its distributed Koopman learning and its MPC integration. During learning, the lifted data matrices are row-partitioned so that each agent  $i \in \mathcal{P}$  processes only local submatrices  $X_i$  and  $Y_i$ . This partitioning reduces per-agent memory to  $\mathcal{O}(n_i N)$ , compared to  $\mathcal{O}(n N)$  centrally, and bounds the computational cost per iteration to  $\mathcal{O}(n_i^2 N)$ , which remains constant under weak scaling as the number of agents  $p$  increases. Communication overhead is minimal since the update rules in (14) exchange only compact summary variables ( $S_i$  and implicitly  $K_i$ ) among neighbors. Consequently, bandwidth requirements depend on the graph connectivity rather than data dimension or sample size.*

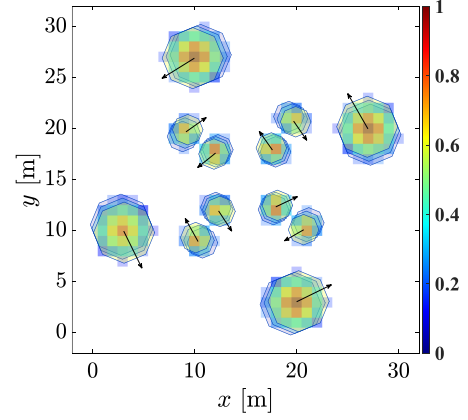


Fig. 9: Predicted intensity–polytope overlays at representative time and its corresponding future horizons.

Convergence is governed by the contraction factor  $\rho_{\max}$ , ensuring that the required iteration count grows only mildly with network size, enabling near-linear wall-clock acceleration with additional agents. In the MPC stage, computational efficiency is maintained when embedding Koopman-based obstacle forecasts into linear constraints. Each predicted obstacle is represented by  $n_\zeta$  supporting half-spaces, with  $n_\zeta = 8$  providing a balanced trade-off between precision and complexity. Enforcing only the most active hyperplane per obstacle and prediction step reduces the number of constraints from  $\mathcal{O}(L_o H n_\zeta)$  to  $\mathcal{O}(L_o H)$  while maintaining conservative safety margins. Because these constraints are linear and preserve the sparsity structure of the nominal dynamics (4), the resulting MPC problems remain tractable and can be efficiently warm-started across iterations. Overall, the framework achieves scalable, real-time operation suitable for high-dimensional, dynamic environments.

#### D. Linking Koopman predictions to MPC constraints via intensity–polytope architecture

To make explicit how perception feeds planning, we visualize the predicted spatial intensities  $\rho_{t+h}$  produced by the distributed Koopman operator and the geometric obstacle sets used by MPC at representative time that coincide with Fig. 6(a). At time  $t$ , the most recent lifted snapshot is propagated forward as  $X_{t+h} \approx K^h X_t$ ,  $h = 1, \dots, H$ , then mapped back to the grid to obtain  $\rho_{t+h} \in [0, 1]$ . For each predicted map, a threshold  $c_\rho$  selects high-likelihood occupancy  $\Psi_t = \{\xi \in \mathbb{R}^2 : \rho_t(\xi) > c_\rho\}$ , to which Gaussian mixture model is fit, yielding centers  $\{\mu_{\ell,t+h}\}$  and covariances  $\{\Sigma_{\ell,t+h}\}$ . Confidence ellipses derived from  $(\mu_{\ell,t+h}, \Sigma_{\ell,t+h})$  are then approximated by polygons and inflated by the safety margin  $\varepsilon$ , producing time-varying polytopes that circumscribe the predicted obstacle mass. Fig. 9 overlays the predicted intensity field  $\rho_{t+h}$ ,  $t = 15$ ,  $h = 1, 7, 14$  to show intensity values inside the union of all nominal polytopes (white background elsewhere) that are passed to MPC as the linear constraints in (32). This view reveals three key connections: (a) the distributed Koopman operator forecasts the future spatial distribution of moving

obstacles on the original grid, (b) the Gaussian mixture model serves as a compact surrogate that locates and shapes obstacle components directly from  $\rho_t$ , and (c) the polygonal circumscribers translate these probabilistic predictions into tractable, conservative linear inequalities enforceable at each step of the MPC horizon. Panels at  $t = 15$  shown in Fig. 9 align with the controller's receding-horizon updates used in Fig. 6(a) for  $h = 1, 7, 14$ . As time progresses, the Koopman predictions advect and deform the intensity ridges, while the Gaussian mixture model components smoothly re-center and re-orient. The resulting polytopes track these changes with  $n_\zeta = 8$  facets, and the inflated boundaries define the actual constraints enforced in (6d). This predictive pipeline explains the anticipatory deviations of the robot path: the controller looks up to the future occupancy through  $\rho_{t+h}$ , receives a compact linear description via the polytopes, and adjusts the trajectory before high-density regions intersect the planned path.

## V. CONCLUSION

This paper has introduced a unified data-driven framework that combines distributed Koopman operator learning with MPC for predictive navigation and dynamic obstacle avoidance. By exploiting high-dimensional sensory information, the proposed approach enables multiple computational nodes to collaboratively model and forecast the motion of surrounding dynamic obstacles without centralized data fusion. The Koopman-based predictions, processed through Gaussian mixture models and polytope approximations, are embedded as linear constraints within the MPC formulation, guaranteeing safe and collision-free operation under uncertainty. The proposed method is inherently scalable and well-suited for ITS applications, where vehicles and infrastructure sensors must cooperate to perceive and react to complex, time-varying environments. The distributed learning algorithm ensures computational efficiency, reduced communication overhead, and real-time adaptability, which are key requirements for future connected and autonomous mobility platforms. Theoretical analysis confirms convergence and consistency of the distributed Koopman estimator, while simulation results demonstrate reliable, safe, and scalable motion planning performance. Overall, this work establishes a foundation for cooperative perception and distributed control in networked transportation systems, advancing the integration of learning-based modeling and control for next-generation autonomous mobility.

## VI. ACKNOWLEDGMENT

The authors are thankful to Marcello Farina for several enlightening discussions on the proposed approach.

## REFERENCES

- [1] C. Yan, Y. Sun, Y. Jiang, X. Xiang, and M. Chen, "Selective imitation enhanced deep reinforcement learning for aav navigation and obstacle avoidance with sparse rewards," *IEEE Transactions on Intelligent Transportation Systems*, 2025.
- [2] J. Tordesillas, B. T. Lopez, M. Everett, and J. P. How, "Faster: Fast and safe trajectory planner for navigation in unknown environments," *IEEE Transactions on Robotics*, vol. 38, no. 2, pp. 922–938, 2021.
- [3] R. Siegwart, I. R. Nourbakhsh, and D. Scaramuzza, *Introduction to autonomous mobile robots*. MIT press, 2011.
- [4] J. B. Rawlings, D. Q. Mayne, M. Diehl *et al.*, *Model predictive control: theory, computation, and design*. Nob Hill Publishing Madison, WI, 2017, vol. 2.
- [5] A. L. Gratzner, M. M. Broger, A. Schirrer, and S. Jakubek, "Two-layer mpc architecture for efficient mixed-integer-informed obstacle avoidance in real-time," *IEEE Transactions on Intelligent Transportation Systems*, vol. 25, no. 10, pp. 13 767–13 784, 2024.
- [6] D. Zhang, D. Huo, M. Zhou, and Z. Cao, "Mpc-ds: A safe path tracking method for agvs in dynamic environments with dense obstacles," *IEEE Transactions on Intelligent Transportation Systems*, 2025.
- [7] M. Farina, A. Perizzato, and R. Scattolini, "Application of distributed predictive control to motion and coordination problems for unicycle autonomous robots," *Robotics and Autonomous Systems*, vol. 72, pp. 248–260, 2015.
- [8] J. Li, X. Xiong, Y. Yan, and Y. Yang, "A survey of indoor uav obstacle avoidance research," *IEEE Access*, vol. 11, pp. 51 861–51 891, 2023.
- [9] M. Li, Z. Sun, Z. Liao, and S. Weiland, "Moving obstacle collision avoidance via chance-constrained mpc with cbf," *arXiv preprint arXiv:2304.01639*, 2023.
- [10] E. Olcay, H. Meeß, and G. Elger, "Dynamic obstacle avoidance for uavs using mpc and gp-based motion forecast," in *2024 European Control Conference (ECC)*. IEEE, 2024, pp. 1024–1031.
- [11] S. X. Wei, A. Dixit, S. Tomar, and J. W. Burdick, "Moving obstacle avoidance: A data-driven risk-aware approach," *IEEE Control Systems Letters*, vol. 7, pp. 289–294, 2022.
- [12] N. Jiang, E. W. M. Lee, X. Li, H. Yu, W. Xie, L. Yang, R. K. K. Yuen, and G. H. Yeoh, "Fam-1stm: predicting macroscopic pedestrian dynamics through data-driven method," *IEEE Transactions on Intelligent Transportation Systems*, 2025.
- [13] W. Mai, D. Duives, P. Krishnakumari, and S. Hoogendoorn, "Evaluating crowd flow forecasting algorithms for indoor pedestrian spaces: A benchmark using a synthetic dataset," *IEEE Transactions on Intelligent Transportation Systems*, 2025.
- [14] Q. Wang, D. Xu, G. Kuang, C. Lv, S. E. Li, and B. Nie, "Risk-aware vehicle trajectory prediction under safety-critical scenarios," *IEEE Transactions on Intelligent Transportation Systems*, 2025.
- [15] Y. Ye, C. Wang, W. Zhao, B. Zhang, and Y. Zhang, "Tp-glif: Trajectory prediction of surrounding vehicles in unsignalized roundabouts based on global-local history information fusion," *IEEE Transactions on Intelligent Transportation Systems*, 2025.
- [16] B. Lindqvist, S. S. Mansouri, A.-a. Agha-mohammadi, and G. Nikolopoulos, "Nonlinear mpc for collision avoidance and control of uavs with dynamic obstacles," *IEEE robotics and automation letters*, vol. 5, no. 4, pp. 6001–6008, 2020.
- [17] T. Zhu, J. Mao, L. Han, C. Zhang, and J. Yang, "Real-time dynamic obstacle avoidance for robot manipulators based on cascaded nonlinear mpc with artificial potential field," *IEEE Transactions on Industrial Electronics*, vol. 71, no. 7, pp. 7424–7434, 2023.
- [18] Z. Xu, H. Shen, X. Han, H. Jin, K. Ye, and K. Shimada, "Lv-dot: Lidar-visual dynamic obstacle detection and tracking for autonomous robot navigation," *arXiv preprint arXiv:2502.20607*, 2025.
- [19] D. Hafner, T. Lillicrap, I. Fischer, R. Villegas, D. Ha, H. Lee, and J. Davidson, "Learning latent dynamics for planning from pixels," in *International conference on machine learning*. PMLR, 2019, pp. 2555–2565.
- [20] I. Mezić, "Analysis of fluid flows via spectral properties of the Koopman operator," *Annual review of fluid mechanics*, vol. 45, no. 1, pp. 357–378, 2013.
- [21] P. Bevanda, S. Sosnowski, and S. Hirche, "Koopman operator dynamical models: Learning, analysis and control," *Annual Reviews in Control*, vol. 52, pp. 197–212, 2021.
- [22] S. E. Otto and C. W. Rowley, "Koopman operators for estimation and control of dynamical systems," *Annual Review of Control, Robotics, and Autonomous Systems*, vol. 4, no. 1, pp. 59–87, 2021.
- [23] M. O. Williams, I. G. Kevrekidis, and C. W. Rowley, "A data-driven approximation of the Koopman operator: Extending dynamic mode decomposition," *Journal of Nonlinear Science*, vol. 25, pp. 1307–1346, 2015.
- [24] J. L. Proctor, S. L. Brunton, and J. N. Kutz, "Dynamic mode decomposition with control," *SIAM Journal on Applied Dynamical Systems*, vol. 15, no. 1, pp. 142–161, 2016.
- [25] C. Gu, T. Zhou, and C. Wu, "Deep Koopman traffic modeling for free-way ramp metering," *IEEE Transactions on Intelligent Transportation Systems*, vol. 24, no. 6, pp. 6001–6013, 2023.

- [26] K. Tian, H. Shi, Y. Zhou, and S. Li, "Physically analyzable ai-based nonlinear platoon dynamics modeling during traffic oscillation: A Koopman approach," *IEEE Transactions on Intelligent Transportation Systems*, 2025.
- [27] G. Gutow and J. D. Rogers, "Koopman operator method for chance-constrained motion primitive planning," *IEEE Robotics and Automation Letters*, vol. 5, no. 2, pp. 1572–1578, 2020.
- [28] A. Comas, S. Ghimire, H. Li, M. Sznaiier, and O. Camps, "Self-supervised decomposition, disentanglement and prediction of video sequences while interpreting dynamics: A koopman perspective," *arXiv preprint arXiv:2110.00547*, 2021.
- [29] X. Zhang, W. Pan, R. Scattolini, S. Yu, and X. Xu, "Robust tube-based model predictive control with Koopman operators," *Automatica*, vol. 137, p. 110114, 2022.
- [30] W. A. Manzoor, S. Rawashdeh, and A. Mohammadi, "Vehicular applications of Koopman operator theory—a survey," *IEEE Access*, vol. 11, pp. 25 917–25 931, 2023.
- [31] H. Zheng, Y. Li, L. Zheng, and E. Hashemi, "Koopman-based hybrid modeling and zonotopic tube robust mpc for motion control of automated vehicles," *IEEE Transactions on Intelligent Transportation Systems*, vol. 25, no. 10, pp. 13 598–13 612, 2024.
- [32] M. Korda and I. Mezić, "Linear predictors for nonlinear dynamical systems: Koopman operator meets model predictive control," *Automatica*, vol. 93, pp. 149–160, 2018.
- [33] S. L. Brunton, J. L. Proctor, and J. N. Kutz, "Discovering governing equations from data by sparse identification of nonlinear dynamical systems," *Proceedings of the national academy of sciences*, vol. 113, no. 15, pp. 3932–3937, 2016.
- [34] Z. Liu, G. Ding, L. Chen, and E. Yeung, "Towards scalable Koopman operator learning: Convergence rates and a distributed learning algorithm," in *2020 American Control Conference (ACC)*. IEEE, 2020, pp. 3983–3990.
- [35] S. P. Nandanoori, S. Pal, S. Sinha, S. Kundu, K. Agarwal, and S. Choudhury, "Data-driven distributed learning of multi-agent systems: A Koopman operator approach," in *2021 60th IEEE Conference on Decision and Control (CDC)*. IEEE, 2021, pp. 5059–5066.
- [36] S. Mukherjee, S. P. Nandanoori, S. Guan, K. Agarwal, S. Sinha, S. Kundu, S. Pal, Y. Wu, D. L. Vrabie, and S. Choudhury, "Learning distributed geometric Koopman operator for sparse networked dynamical systems," in *Learning on Graphs Conference*. PMLR, 2022, pp. 45–1.
- [37] W. Hao, L. Wang, A. Rai, and S. Mou, "Distributed deep Koopman learning for nonlinear dynamics," *arXiv preprint arXiv:2409.11586*, 2024.
- [38] W. Hao, Z. Lu, D. Upadhyay, and S. Mou, "A distributed deep Koopman learning algorithm for control," *arXiv preprint arXiv:2412.07212*, 2024.
- [39] A. Azarbahram, S. Liu, and G. P. Incremona, "Distributed Koopman operator learning from sequential observations," *arXiv preprint arXiv:2509.20071*, 2025.
- [40] V. Bueno, A. Azarbahram, M. Farina, and L. Fagiano, "Koopman-based dynamic environment prediction for safe uav navigation," *arXiv preprint arXiv:2511.06990*, 2025.
- [41] A. Azarbahram, C. P. Y. Huanca, G. P. Incremona, and P. Colaneri, "Distributed switching model predictive control meets koopman operator for dynamic obstacle avoidance," *arXiv preprint arXiv:2511.17186*, 2025.
- [42] G. Oriolo, A. De Luca, and M. Vendittelli, "Wmr control via dynamic feedback linearization: design, implementation, and experimental validation," *IEEE Transactions on control systems technology*, vol. 10, no. 6, pp. 835–852, 2002.
- [43] S. Boyd and L. Vandenberghe, *Convex Optimization*. Cambridge University Press, 2004.
- [44] S. Liu, "Scalable distributed least squares algorithm for linear algebraic equations via scheduling," *arXiv preprint arXiv:2411.06883*, 2024.
- [45] H. Zhang, C. W. Rowley, E. A. Deem, and L. N. Cattafesta, "Online dynamic mode decomposition for time-varying systems," *SIAM Journal on Applied Dynamical Systems*, vol. 18, no. 3, pp. 1586–1609, 2019.